DR LUCIENNE BUANNIC (Orcid ID : 0000-0003-3055-4058)

PROFESSOR KATHERINE T FABER (Orcid ID : 0000-0001-6585-2536)

Article type : Article

Title

Dense Freeze-cast $Li_7La_3Zr_2O_{12}$ Solid Electrolytes with Oriented Open Porosity and Contiguous Ceramic Scaffold

Authors

Lucienne Buannic,[1]* Maninpat Naviroj,[2] Sarah M. Miller,[2] Jakub Zagorski,[1] Katherine T. Faber,[2,3] and Anna Llordés[1,4]*

[1] CIC Energigune, Parque Tecnológico de Alava, Miñano 01510, Spain

[2] Department of Materials Science and Engineering, Northwestern University, Evanston, IL 60208, United States

[3] Division of Engineering and Applied Science, California Institute of Technology, Pasadena, CA 91125, United States

[4] IKERBASQUE, The Basque Foundation for Science, Maria Diaz de Haro 3, 48013 Bilbao, Spain

* Corresponding authors: lbuannic@cicenergigune.com; allordes@cicenergigune.com

Abstract

Freeze casting is used for the first time to prepare solid electrolyte scaffolds with oriented porosity and dense ceramic walls made of $Li_7La_3Zr_2O_{12}$ (LLZO), one of the most promising candidates for solid state battery electrolytes. Processing parameters - such as solvent solidification rate, solvent type, and ceramic particle size - are investigated, focusing on their influence on porosity and ceramic wall density. Dendrite-like porosity is obtained when using cyclohexane and dioxane as solvents. Lamellar porosity is observed in aqueous slurries resulting in a structure with the highest apparent porosity and densest ceramic scaffold but weakest mechanical properties due to the lack of interlamellar support. The use of smaller LLZO particle size in the slurries resulted in lower porosity and denser ceramic walls. The intrinsic ionic conductivity of the oriented LLZ ceramic scaffold is unaffected by the freeze casting technique, providing a promising ceramic scaffold for polymer infill in view of designing new types of ceramic-polymer composites.

Keywords

$Li_7La_3Zr_2O_{12}$; solid state batteries; freeze casting; porous ceramic scaffold; composite electrolyte

1. Introduction

Following a series of safety issues related to the use of current Li-ion battery (LIB) technologies, replacement of the flammable and toxic organic liquid electrolyte by a solid state electrolyte has recently attracted much interest.[1, 2] Solid state electrolytes for LIB applications require a material with high ionic conductivity, high density, and high chemical/electrochemical stability. Proposed contenders include oxide- and sulfide-based materials as well as polymers. Sulfides offer the highest ionic conductivities but with poor chemical and narrow electrochemical

stability windows,[3-5] while polymers provide high mechanical flexibility but poor ionic conductivities.[6] Ceramic oxides, and in particular $Li_7La_3Zr_2O_{12}$ (LLZO), offer high ionic conductivity with the best chemical and widest electrochemical stability window;[3-5] however they can be difficult to densify.[7-9] Additionally, bulk ceramic oxides are usually stiff and the solid/solid interface between the ceramic electrolyte and the cathode are characterized by high interfacial resistances.[10, 11] One way to overcome these inherent limitations is to combine ceramic oxides with polymers to yield a composite structure. Ideally, the ceramic-polymer composite would benefit from the high ionic conductivity of the ceramic oxide while gaining the flexibility of the polymer.

The typical approach to prepare ceramic-polymer composites is based on mixing the two materials and tape-casting the composite slurry, which results in a flexible membrane with ceramic particles dispersed in a polymer matrix (Figure 1a). However, the noncontiguous network of ceramic particles forces the lithium ions to diffuse through the polymer matrix, limiting the overall ionic conductivity.[12-18] In order to benefit from the high ionic conductivity of the ceramic, new composite architectures providing a percolative ceramic network need to be designed. The use of ceramic electrospun nanofibers is one way to increase the length of the percolative ceramic network.[14, 19] However the nanofibers are typically oriented along the membrane plane and fail to provide a continuous ceramic percolative network along the conduction direction in the battery application, i.e. perpendicular to the membrane plane. The nanofibers also tend to be randomly distributed within the polymer matrix, resulting in aggregation and resistive interconnections detrimental for reaching high ionic conductivity. Ensuring a contiguous ceramic scaffold perpendicular to the membrane plane would be ideal, but such complex architectures cannot be prepared by conventional mixing (Figure 1a). To prepare a composite with a contiguous ceramic scaffold, one could infill the residual porosity present after partial sintering of a bulk ceramic by a polymer. However the disordered and closed nature of the porous network limits the capability for infiltration (Supporting Figure S1). To circumvent such limitation, here we report the use of freeze casting, also

known as ice templating, to induce open porosity in a contiguous complex oxide scaffold, providing ionic conduction pathways oriented along the conduction direction.

Freeze casting allows templating of a solid structure with a high degree of open and ordered porosity via the solidification of a solvent-based slurry (Figure 1b). The first step of freeze casting consists in the preparation of a stable suspension of the ceramic particles in a solvent. Controlled solidification of the suspension leads to the segregation of the ceramic particles (in the suspension) in between the growing crystals of solvent. After sublimation of the solidified solvent via freeze drying, the resulting porosity/pore structure is the negative image of the solvent crystals. The pores can be directionally oriented when the solidification process occurs unidirectionally. Finally, high temperature sintering ensures consolidation and densification of the ceramic scaffold while retaining the larger interconnected pores prior to their infiltration with a polymer.

Porous alumina was the first porous ceramic to be templated using freeze casting.[20] To date, this technique has been applied to naturally occurring minerals, binary oxides or their composite, such as hydroxyapatite, silica and zirconia, to obtain solids with controlled porosity for application in bone regeneration, filtration media, catalyst support or thermal insulation.[21-23] The technique has also been applied to the preparation of bi-layer thin films for solid oxide fuel cells,[24] which highlights its versatility. While the most common solvent or dispersion medium used for freeze casting is water,[21] solvents such as camphene, tert-butyl alcohol, cycloalkanes, dioxane or dimethyl carbonate [21, 23, 25] have also been employed, providing alternatives to water for moisture-sensitive ceramics, as is the case for most Li-ion solid electrolytes.[26, 27]

Ice templating has recently been applied to $Li_{1+x}Al_xTi_{2-x}(PO_4)_3$, demonstrating the feasibility of freeze casting on solid electrolyte candidates.[28] However this material provides a narrow electrochemical stability window, due to the presence of Ti^{4+} which can be reduced in contact with the anode, and poor ionic conductivity.[6] In this study, $Li_7La_3Zr_2O_{12}$ (LLZO) was chosen as the complex oxide ceramic scaffold. In its cubic phase, the material provides the highest Li^+ conductivity reported

for oxide ceramics,[29-32] with 10^{-3} S·cm^{-1}, as well as the largest electrochemical stability window amongst the Li-ion conductors.[4, 5] However, ultra dry environments are required to guarantee stability and high ionic conductivity of the cubic phase.[29] To assess the feasibility of the technique without the requirement to work under a constraining controlled atmosphere, the tetragonal LLZO garnet phase, which exhibits a total ionic conductivity of ≈ 10^{-7} S·cm^{-1}, instead of the cubic phase was employed to prepare the freeze cast solids .[33] Herein, we investigate the technique of freeze casting to create a contiguous and dense ceramic scaffold of tetragonal LLZO with open and oriented porosity (Figure 1b). The effects of solvent type, solidification rate, and ceramic particle size on the resulting porosity are evaluated. The ionic conductivity of selected porous solids is compared to that of a pellet prepared via conventional uniaxial pressing.

2. Experimental Methods

$Li_7La_3Zr_2O_{12}$ powder was prepared by a sol-gel route using $LiNO_3$ (Reagent plus, Sigma-Aldrich), $La(NO_3)_3{\cdot}6\ H_2O$ (>99.0%, Fluka), and $Zr(C_5H_7O_2)_4$ (Alfa Aesar). Stoichiometric amounts of starting materials – with a 10 mol.% $LiNO_3$ excess to compensate for Li evaporation during the sintering phase – were placed in a porcelain dish. Citric acid (>99.0%, Sigma-Aldrich) previously dissolved in a minimum amount of distilled water was added to the reagent mixture, with a citric acid to cation molar ratio of 4:1. After dissolution, the solution was dehydrated on a hot plate and the resulting gel was then annealed at 600°C for 12 h to decompose the organic components. The resulting powder was ground and heated to 800°C for 12 h under dry O_2 (H_2O content < 1 ppm). After thermal treatment, the powder was manually ground. To assess the effect of particle size, some of the powder was ball milled in isopropanol for 25 min at 500 rpm using a Fristsch Pulverisette 7.

X-ray diffraction (XRD) was performed using a Bruker-D8 diffractometer (Cu source with Kα1 and Kα2, accelerating voltage of 30 kV, and current of 50 mA) in the Bragg−Brentano geometry; data were collected from 15 to 80° 2θ, with a 0.02° step size. Particle size distribution of the powder was analyzed with a Mastersize 3000 Malvern equipped with a Hydro MV wet powder disperser. The powder was suspended in ethanol and continuously mixed during the measurement.

Slurries containing $Li_7La_3Zr_2O_{12}$ ceramic powder, a solvent, and a dispersant were prepared in 1 mL batches. The weight fraction of dispersant to ceramic was fixed to 0.03. The typical ceramic loading in the slurry was 20 vol.%; additional trials were conducted with 30 and 40 vol. %. Three solvents were used for comparison: cyclohexane (m.p. = 6°C, Sigma–Aldrich), dioxane (m.p. = 12°C, Sigma–Aldrich) and distilled water. Fish oil (Sigma Aldrich) was used as a dispersant for cyclohexane- and dioxane-based slurries while Darvan 811 (Vanderbilt Minerals) was used with water. The slurries were ball milled overnight prior to casting.

The freeze casting setup consisted of a water-cooled thermoelectric plate placed at the base of a cylindrical glass mold (inner diameter: 8 mm) into which the slurry, at a temperature of 25°C, was poured. Prior to pouring, the thermoelectric temperature was set to 10°C, 15°C, and -3°C for cyclohexane-, dioxane-, and water- based slurries, respectively. After pouring, the thermoelectric temperature was lowered with a ramping rate of $3°C \cdot min^{-1}$ to -30°C for cyclohexane and dioxane and -40°C for water. One of the cyclohexane-based slurries was also quenched to -30°C after pouring.

After solidification, the samples were placed in a 1 L FreeZone freeze dryer (Labconco,) at −50°C and <0.100 mBar for 24 h, until all the solvent was sublimed. After removal of the mold, the remaining solids were buried in MgO powder (Sigma Aldrich 98%) and sintered at 1150°C for 6 h under argon. The amount of apparent porosity and the LLZO percent theoretical density of the scaffold were measured for the sintered freeze-cast solids using Archimedes' method and the theoretical density value of $Li_7La_3Zr_2O_{12}$ ($5.11\ g\ cm^{-3}$).

The sintered solids had an approximate diameter and height of 6 and 7 mm, respectively. The top layer of the solids was cut with a slow speed diamond saw in order to observe the transverse cross section of the solids, i.e. perpendicular to the freezing direction. Longitudinal cross sections were also evaluated after cutting the solid along the freezing direction. Microstructure of the freeze-cast solids was analyzed by scanning electron microscopy (SEM) using a ZEISS 1550VP FESEM.

Electrochemical impedance spectroscopy measurements (EIS) were carried out using a Solartron 1260A Impedance Analyzer with frequencies ranging between 32 MHz and 1 Hz and with a 50 mV excitation amplitude. The freeze-cast solids were sandwiched between two Li metal disks and assembled in a Swagelok cell. As a reference, a 6 mm diameter pellet was uniaxially pressed to 1.5 tons and sintered under the same conditions as the freeze-cast solids prior to measuring its ionic conductivity. The Nyquist plots were fitted using an equivalent circuit model to obtain the solid resistance and the ionic conductivity was determined using the following equation:

$$\sigma_i = \frac{l}{A} \cdot \frac{1}{R} \qquad (1)$$

where l, A, and R are the thickness, area, and resistance of the electrolyte, respectively.

3. Results and Discussion

The as-prepared $Li_7La_3Zr_2O_{12}$ (LLZO) powder crystallizes in a tetragonal phase with space group $I4_1/acd$ (142) (Figure 2a).[33] The presence of some $La_2Zr_2O_7$ and La_2O_3 indicates an incomplete reaction after the thermal treatment at 800°C. A higher thermal treatment would be needed to obtain a pure $Li_7La_3Zr_2O_{12}$ phase; however this would likely lead to particle growth prior to final sintering, which could be detrimental to the preparation of solids with oriented porosity as it will be demonstrated below. After sintering of the solids, the disappearance of the secondary phases along with a phase transformation from tetragonal to cubic are observed (Figure 2a). The as-prepared

powder presents a particle size distribution Dv50 of 18 µm (Figure 2b). A ball-milling treatment allows reducing the particle size to a Dv50 of 1.4 µm. The effect of the particle size on the freeze-cast solids will be discussed below.

Rapid solidification of the cyclohexane-based slurry (20 vol.% ceramic) via quenching leads to a homogenous distribution of the ceramic particles and pores in both the transverse and longitudinal planes: no pore directionality is observed (Supporting Figure S2). In the case of rapid solidification, the particles are entrapped in the solidification front and the solvent crystals grow in the interparticle spaces leading to a homogenous distribution of the ceramic particles and porosity.[34] To obtain directional porosity, the ceramic particles need to be rejected from the solidification front. The solvent crystals can then grow into the slurry while the ceramic particles are concentrated in between the growing crystals of solvent.[34] It is therefore necessary to lower the solidification rate of the slurry below the critical velocity for particle entrapment to create directional porosity.

Solid samples prepared with cyclohexane, dioxane, and water (with 20 vol.% ceramic content in the slurry) all show a continuous pore network in their longitudinal cross section when cooled at 3°C·min^{-1} (Figure 3). The use of cyclohexane and dioxane results in the presence of dendrite-like pores with a diameter of ≈ 20 µm (Figure 3 a - d). In the case of dioxane (Figure 3 c, d), the dendrite-like pores tend to align with one another, possibly due to the coalescence of their secondary branches. When water was used (Figure 3 e, f), a lamellar porosity is obtained with a wall thickness between 5 and 30 µm and an interwall distance of 10 to 40 µm. The mechanical properties of the solid prepared with water were poor due to the lack of interlamellar support resulting in a fragile solid that collapsed when handled. As a consequence, water as a solvent was discarded for further experimental investigation in this study. This result is in clear contradiction with the flexibility reported for ice-templated $Li_{1+x}Al_xTi_{2-x}(PO_4)_3$,[28] a material that seem to offer higher mechanical properties. For all freeze cast samples in Figure 3, the openness of the porosity network is clearly visible along the freezing direction (longitudinal cross-section) for all solvents, indicating the

presence of directional porosity. Increase of the solid loadings to 30 vol.% and above leads to the disappearance of the macroporous network (Supporting Figure S3). The use of a smaller particle size would be preferred for higher solid loadings.

For slurries prepared with cyclohexane or dioxane with 20 vol.% ceramic content, decreasing the particle size of the ceramic powder significantly affects the morphology of the freeze-cast ceramic scaffolds and the volume fractions of apparent porosity (Figure 4). For the cyclohexane-based slurry, the diameter of the pores decreases to ≈ 10 µm (Figure 4 a, b), half of the size observed with the larger particle size (Figure 3 a, b). In the case of the dioxane-based slurry, the alignment of the dendrite-like pores becomes even more obvious (Figure 4 c, d), with an average pore diameter of ≈ 40 µm, twice as large as the pores observed with the larger particle size (Figure 3 c, d). As a result, the ceramic scaffold appears thicker and denser which should lead to a higher density of the ceramic skeleton.

Density and porosity measurements of the sintered solids were performed following Archimedes' method (Table 1). For a larger particle size, the quenched cyclohexane-based slurry provides a similar apparent porosity (65%) to the cyclohexane- and dioxane-based slurries cooled at 3°C·min^{-1} (61 and 57%, respectively). The quenched solid does not offer directional porosity as discussed above, but the percent theoretical density of the LLZO scaffold is higher (87%) than that of the slowly cooled solids (76 and 68% for cyclohexane and dioxane respectively). The homogenous distribution of ceramic particles in the quenched solid results in the presence of larger pores after solvent removal, the large pores remaining open post-sintering. In comparison, smaller pores present in the ceramic walls of the slowly cooled solids are more likely to become closed after sintering, decreasing the density of the ceramic scaffold. The water-based slurry provides the highest apparent porosity (75%) with the highest percent theoretical density of the LLZO ceramic walls (93%). Expansion of water during freezing leads to further compaction of the LLZO particles between

adjacent ice crystals and decreases the ceramic wall pore size upon slurry solidification. Removal of these small pores via sintering results in more dense ceramic walls.

With a smaller particle size (from a Dv50 of 18 to 1.4 µm), the LLZO percent theoretical density increases by 20-30% while the apparent porosity decreases by 10-20% in the cyclohexane- and dioxane-based slurries cooled at 3°C·min^{-1} (Table 1 and Figure 4).The former suggests better compaction of the LLZO particles into ceramic walls during freeze casting since all the slurries presented in Table 1 were prepared with a ceramic loading of 20 vol.%. The dioxane-based slurry leads to a slightly larger amount of closed porosity in the LLZO scaffold, possibly due to the presence of smaller secondary branches during crystallization of the solvent[25] which are more likely to become closed pores after sintering in comparison to the thick primary branches.

The freeze-cast solids prepared using cyclohexane-based slurries (20 vol.%) are characterized by higher LLZO densities in comparison to the ones prepared with dioxane; therefore they were selected to correlate the changes in solid properties due to ceramic particle size on the ionic conductivity of the freeze cast solids. The room temperature ionic conductivities of the two samples prepared in air were determined by fitting the Nyquist plot with the equivalent circuit shown in Figure 5, leading to $\sigma_{i,RT}$ of 1.1 x 10^{-7} and 1.3 x 10^{-7} S·cm^{-1} for a Dv50 of 18 and 1.4 µm, respectively (Table 2). In comparison, a sintered pellet uniaxially pressed (16% apparent porosity and 85% LLZO percent theoretical density) prepared using the LLZO powder with a Dv50 of 18 µm is characterized by an ionic conductivity of 2.3 x 10^{-7} S·cm^{-1} at room temperature (Figure 5 and Table 2). Taking into consideration the apparent porosity of the pellet (16%), an ionic conductivity of 2.7 x 10^{-7} S·cm^{-1} is extrapolated to that expected in the absence of apparent porosity. In the case of the freeze-cast LLZO solids, the extrapolated values are similar with 2.8 x 10^{-7} and 2.6 x 10^{-7} S·cm^{-1} for a Dv50 of 18 and 1.4 µm, respectively. The comparable conductivity values obtained for the three samples indicate that the ionic transport within the ceramic scaffold (dense wall) itself is not affected by freeze casting. Therefore, the technique could be applied under controlled atmosphere to prepare

porous ceramic scaffolds with higher ionic conductivities such as that with a cubic LLZO powder unexposed to air.[35] Additionally, infiltration of the porosity by a polymer solution is demonstrated (Figure 6) showing good promise for future preparation of oriented ceramic-polymer composites. From the viewpoint of practical application in solid state batteries, obtaining thin composite solids (thickness < 50 μm) will be a key challenge to further develop this promising composite architecture. A post-preparation cutting step could allow precise thinning of the electrolyte layer within the limit of the cutting technique employed and the mechanical properties of the composite solid.

4. Conclusions

Freeze casting enabled the preparation of dense $Li_7La_3Zr_2O_{12}$ garnet scaffolds with directional open porosity. Scaffolds prepared with cyclohexane- and dioxane-based LLZO slurries showed a dendrite-like porous network, with some degree of pore alignment in the case of dioxane, while the scaffold prepared from a water-based slurry presented lamellar porosity. The solid prepared with a water-based slurry is characterized by the highest amount of apparent porosity (75%) and the highest LLZO percent theoretical density (93%); however, the solid was found difficult to handle due to the lack of interlamellar support. The rate of slurry solidification is shown to be an important parameter in controlling the directionality and ordering of the porous network. Solidification by quenching of a cyclohexane-based slurry results in the homogenous distribution of porosity and the absence of directionality. Decreasing the particle size of the LLZO powder for cyclohexane- and dioxane-based slurries leads to a denser ceramic scaffold but lower apparent porosity. The solids prepared with cyclohexane-based slurries have an ionic conductivity in the range of 10^{-7} $S \cdot cm^{-1}$ which is comparable to the ionic conductivity of uniaxially pressed and sintered tetragonal LLZO, if taking into consideration the amount of apparent porosity. This similar conductivity indicates that solids prepared by freeze casting under controlled atmosphere could provide a competitive ionic conductivity if prepared with LLZO garnet powder unexposed to air.

Subsequent infiltration of the porous LLZO scaffold with a Li^+ conductive polymer electrolyte would provide a ceramic-polymer composite with at least two different ionic pathways (one via the ceramic and one through the polymer) oriented parallel to the ionic motion of a solid state battery. This novel design, based on a dense and oriented ceramic pathway, could offer new strategies to improve the ionic conductivity in ceramic-polymeric composites via ceramic freeze casting followed by polymer infill.

Acknowledgments

This work was conducted at Caltech (USA) and CIC Energigune (Spain) within the framework of a Jose Castillejo mobility fellowship from the Spanish Ministry of Education, Culture, and Sports received by L.B. This work was also supported by the Basque government through the ELKARTEK 15 program. A.L. acknowledges financial support from IKERBASQUE. K.T.F. and M.N. acknowledge the support of the US National Science Foundation through DMR-1411218. L.B. also thanks Dr. Matthew Johnson and Neal Brodnik for helpful discussions.

References

1. Janek J, Zeier WG. A solid future for battery development. Nat Energy. 2016; 1:16141.

2. Varzi A, Raccichini R, Passerini S, Scrosati B. Challenges and prospects of the role of solid electrolytes in the revitalization of lithium metal batteries. J Mater Chem A. 2016; 4 (44):17251-17259.

3. Han F, Zhu Y, He X, Mo Y, Wang C. Electrochemical stability of $Li_{10}GeP_2S_{12}$ and $Li_7La_3Zr_2O_{12}$ solid electrolytes. Adv Energy Mater. 2016; 6 (8):1501590-n/a.

4. Richards WD, Miara LJ, Wang Y, Kim JC, Ceder G. Interface stability in solid-state batteries. Chem Mater. 2016; 28 (1):266-273.

5. Zhu Y, He X, Mo Y. First principles study on electrochemical and chemical stability of solid electrolyte-electrode interfaces in all-solid-state li-ion batteries. J Mater Chem A. 2016; 4 (9):3253-3266.

6. Bekaert E, Buannic L, Lassi U, Llordés A, Salminen J. Electrolytes for Li- and Na-ion batteries: Concepts, candidates, and the role of nanotechnology. Elsevier: 2017.

7. Janani N, Deviannapoorani C, Dhivya L, Murugan R. Influence of sintering additives on densification and Li^+ conductivity of al doped $Li_7La_3Zr_2O_{12}$ lithium garnet. RSC Adv. 2014; 4 (93):51228-51238.

8. Janani N, Ramakumar S, Kannan S, Murugan R. Optimization of lithium content and sintering aid for maximized Li^+ conductivity and density in Ta-doped $Li_7La_3Zr_2O_{12}$. J Am Ceram Soc. 2015; 98 (7):2039-2046.

9. Wang Y, Yan P, Xiao J, Lu X, Zhang J-G, Sprenkle VL. Effect of Al_2O_3 on the sintering of garnet-type $Li_{6.5}La_3Zr_{1.5}Ta_{0.5}O_{12}$. Solid State Ionics. 2016; 294:108-115.

10. Sharafi A, Meyer HM, Nanda J, Wolfenstine J, Sakamoto J. Characterizing the Li–$Li_7La_3Zr_2O_{12}$ interface stability and kinetics as a function of temperature and current density. J Power Sources. 2016; 302:135-139.

11. Aguesse F, Manalastas W, Buannic L, Lopez del Amo JM, Singh G, Llordes A, et al. Investigating the dendritic growth during full cell cycling of garnet electrolyte in direct contact with Li metal. ACS Appl Mater Inter. 2017; 9:3808–3816.

12. Choi J-H, Lee C-H, Yu J-H, Doh C-H, Lee S-M. Enhancement of ionic conductivity of composite membranes for all-solid-state lithium rechargeable batteries incorporating tetragonal $Li_7La_3Zr_2O_{12}$ into a polyethylene oxide matrix. J Power Sources. 2015; 274:458-463.

13. Jung Y-C, Lee S-M, Choi J-H, Jang SS, Kim D-W. All solid-state lithium batteries assembled with hybrid solid electrolytes. J Electrochem Soc. 2015; 162 (4):A704-A710.

14. Liu W, Liu N, Sun J, Hsu P-C, Li Y, Lee H-W, et al. Ionic conductivity enhancement of polymer electrolytes with ceramic nanowire fillers. Nano Lett. 2015; 15 (4):2740-2745.

15. Jung Y-C, Kim S-K, Kim M-S, Lee J-H, Han M-S, Kim D-H, et al. Ceramic separators based on Li^+-conducting inorganic electrolyte for high-performance lithium-ion batteries with enhanced safety. J Power Sources. 2015; 293:675-683.

16. Buvana P, Vishista K, Shanmukaraj D, Murugan R. Lithium garnet oxide dispersed polymer composite membrane for rechargeable lithium batteries. Ionics. 2016:1-8.

17. Jung Y-C, Park M-S, Doh C-H, Kim D-W. Organic-inorganic hybrid solid electrolytes for solid-state lithium cells operating at room temperature. Electrochim Acta. 2016; 218:271-277.

18. Langer F, Bardenhagen I, Glenneberg J, Kun R. Microstructure and temperature dependent lithium ion transport of ceramic–polymer composite electrolyte for solid-state lithium ion batteries based on garnet-type $Li_7La_3Zr_2O_{12}$. Solid State Ionics. 2016; 291:8-13.

19. Fu K, Gong Y, Dai J, Gong A, Han X, Yao Y, et al. Flexible, solid-state, ion-conducting membrane with 3D garnet nanofiber networks for lithium batteries. P Natl Acad Sci USA. 2016; 113 (26):7094-7099.

20. Fukasawa T, Ando M, Ohji T, Kanzaki S. Synthesis of porous ceramics with complex pore structure by freeze-dry processing. J Am Ceram Soc. 2001; 84 (1):230-232.

21. Deville S. Freeze-casting of porous ceramics: A review of current achievements and issues. Adv Eng Mater. 2008; 10 (3):155-169.

22. Miller SM, Xiao X, Faber KT. Freeze-cast alumina pore networks: Effects of freezing conditions and dispersion medium. J Eur Ceram Soc. 2015; 35 (13):3595-3605.

23. Naviroj M, Miller SM, Colombo P, Faber KT. Directionally aligned macroporous SiOC via freeze casting of preceramic polymers. J Eur Ceram Soc. 2015; 35 (8):2225-2232.

24. Moon J-W, Hwang HJ, Awano M, Maeda K, Kanzaki S. Preparation of dense thin-flm solid electrolyte on novel porous structure with parallel pore channel. J Ceram Soc Jpn. 2002; 110 (1281):479-484.

25. Naviroj M, Voorhees PW, Faber KT. Suspension- and solution-based freeze casting for porous ceramics. J Mater Res. 2017; 32 (17):3372-3382.

26. Galven C, Fourquet J-L, Crosnier-Lopez M-P, Le Berre F. Instability of the lithium garnet $Li_7La_3Sn_2O_{12}$: Li^+/H^+ exchange and structural study. Chem Mater. 2011; 23 (7):1892-1900.

27. Larraz G, Orera A, Sanz J, Sobrados I, Diez-Gomez V, Sanjuan ML. NMR study of Li distribution in $Li_{7-x}H_xLa_3Zr_2O_{12}$ garnets. J Mater Chem A. 2015; 3 (10):5683-5691.

28. Zhai H, Xu P, Ning M, Cheng Q, Mandal J, Yang Y. A flexible solid composite electrolyte with vertically aligned and connected ion-conducting nanoparticles for lithium batteries. Nano Lett. 2017; 17 (5):3182-3187.

29. Bernuy-Lopez C, Manalastas W, Lopez del Amo JM, Aguadero A, Aguesse F, Kilner JA. Atmosphere controlled processing of Ga-substituted garnets for high Li-ion conductivity ceramics. Chem Mater. 2014; 26 (12):3610-3617.

30. Rettenwander D, Redhammer G, Preishuber-Pflügl F, Cheng L, Miara L, Wagner R, et al. Structural and electrochemical consequences of Al and Ga cosubstitution in $Li_7La_3Zr_2O_{12}$ solid electrolytes. Chem Mater. 2016; 28 (7):2384-2392.

31. Wu J-F, Chen E-Y, Yu Y, Liu L, Wu Y, Pang WK, et al. Gallium-doped $Li_7La_3Zr_2O_{12}$ garnet-type electrolytes with high lithium-ion conductivity. ACS Appl Mater Inter. 2017; 9:1542–1552.

32. Buannic L, Orayech B, López Del Amo J-M, Carrasco J, Katcho NA, Aguesse F, et al. Dual substitution strategy to enhance Li^+ ionic conductivity in $Li_7La_3Zr_2O_{12}$ solid electrolyte. Chem Mater. 2017; 29 (4):1769-1778.

33. Awaka J, Kijima N, Hayakawa H, Akimoto J. Synthesis and structure analysis of tetragonal $Li_7La_3Zr_2O_{12}$ with the garnet-related type structure. J Solid State Chem. 2009; 182 (8):2046-2052.

34. Chino Y, Dunand DC. Directionally freeze-cast titanium foam with aligned, elongated pores. Acta Mater. 2008; 56 (1):105-113.

35. Yow ZF, Oh YL, Gu W, Rao RP, Adams S. Effect of Li^+/H^+ exchange in water treated Ta-doped $Li_7La_3Zr_2O_{12}$. Solid State Ionics. 2016; 292:122-129.

Figure Catpions

Figure 1. Comparison of ceramic-polymer composites obtained via a state of the art approach or freeze casting: (a) Conventional solvent dispersion and tape-casting approach leading to a non-contiguous and disordered ceramic network, (b) Freeze casting approach leading to a dense ceramic scaffold with a contiguous and oriented porosity which can later be infiltrated with a polymer (adapted from Miller[22]).

Figure 2. Characterization of the $Li_7La_3Zr_2O_{12}$ powder: (a) XRD pattern before ball-milling showing the tetragonal LLZO main phase and secondary phases and the cubic LLZO after sintering, (b) Particle size distribution of the as-prepared powder and after ball-milling.

Figure 3. Effect of the solvent on the porous network of the freeze-cast $Li_7La_3Zr_2O_{12}$ solid prepared using a powder with a Dv50 of 18 µm. Transverse (a, c, e) and longitudinal (b, d, f) cross sectional SEM views of cyclohexane- (a, b), dioxane- (c, d), and water- (e, f) based slurries (20 vol.% LLZO) cooled at a rate of $3°C \cdot min^{-1}$.

Figure 4. Effect of the particle size on the porous network of the freeze-cast $Li_7La_3Zr_2O_{12}$ solid prepared using a powder with a Dv50 of 1.4 µm. Transverse (a, c) and longitudinal (b, d) cross sectional SEM views of cyclohexane- (a, b) and dioxane- (c, d) based slurries (20 vol.% LLZO) cooled at a rate of $3°C \cdot min^{-1}$.

Figure 5. Electrochemical characterization of the freeze-cast LLZO solids: Nyquist plots of freeze-cast $Li_7La_3Zr_2O_{12}$ solids (red dots/line and blue triangles/line) compared to a conventional pellet (black squares/line). The symbols represent the experimental data and the solid lines correspond to the fitting using the represented model.

Figure 6. Longitudinal cross sectional view along a fracture surface of the polymer-infiltrated $Li_7La_3Zr_2O_{12}$ freeze-cast solid, showing the ceramic scaffold and the polymer network. Scanning electron microscopy images acquired with (a) secondary electrons and (b) backscattered electrons. The white arrow on the images indicates the freezing direction. The solid was prepared with a cyclohexane-based slurry (20 vol. % LLZ) cooled at a rate of $3°C \cdot min^{-1}$.

Table 1. Summary of the freeze casting parameters and microstructural characteristics of the resulting LLZO porous solids prepared with 20 vol.% of ceramic in the slurry.

Solvent	Cyclohexane	Cyclohexane	Cyclohexane	Dioxane	Dioxane	Water
Cooling Rate ($°C \cdot min^{-1}$)	quenched	3	3	3	3	3
Dv50 (µm)	18	18	1.4	18	1.4	18
Apparent Porosity (%)	65	61	50	57	51	75
LLZO Percent Theoretical Density (%)	87	76	94	68	89	93

Table 2. Characteristics of the solids assessed by electrochemical impedance spectroscopy.

	Uniaxially pressed and sintered pellet	Freeze cast (20 vol. % LLZ in cyclohexane under ambient atmosphere) and sintered solids	
Dv50 (µm)	18	18	1.4
Apparent Porosity (%)	16	61	50
LLZO Percent Theorotical Density (%)	85	76	94
$\sigma_{i,RT}$ ($S \cdot cm^{-1}$)	2.3×10^{-7}	1.1×10^{-7}	1.3×10^{-7}
$\sigma_{i,RT}$ extrapolated to no apparent porosity ($S \cdot cm^{-1}$)	2.7×10^{-7}	2.8×10^{-7}	2.6×10^{-7}

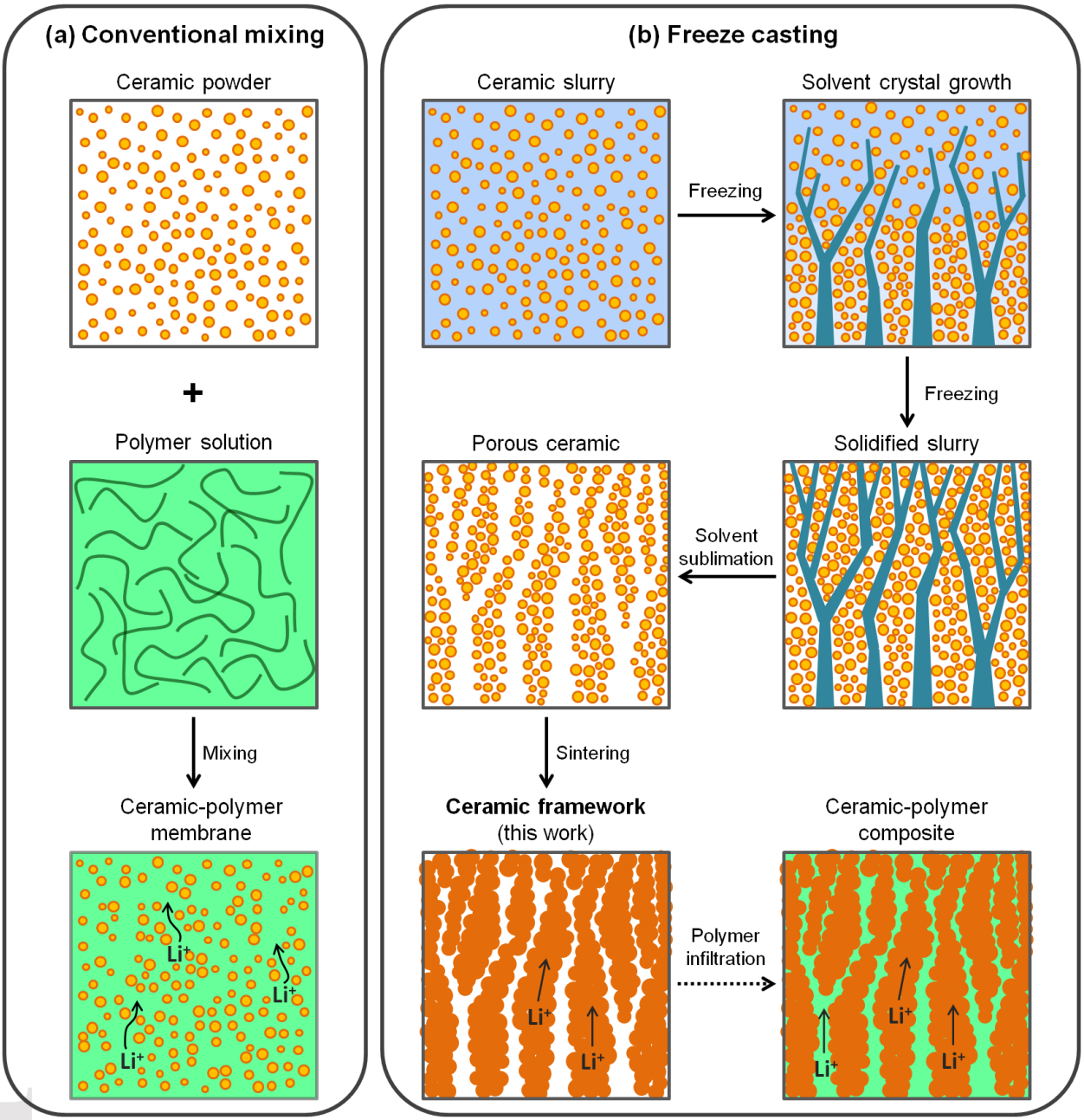

Figure 1. Comparison of ceramic-polymer composites obtained via a state of the art approach or freeze casting: (a) Conventional solvent dispersion and tape-casting approach leading to a non-contiguous and disordered ceramic network, (b) Freeze casting approach leading to a dense ceramic scaffold with a contiguous and oriented porosity which can later be infiltrated with a polymer (adapted from Miller[22]).

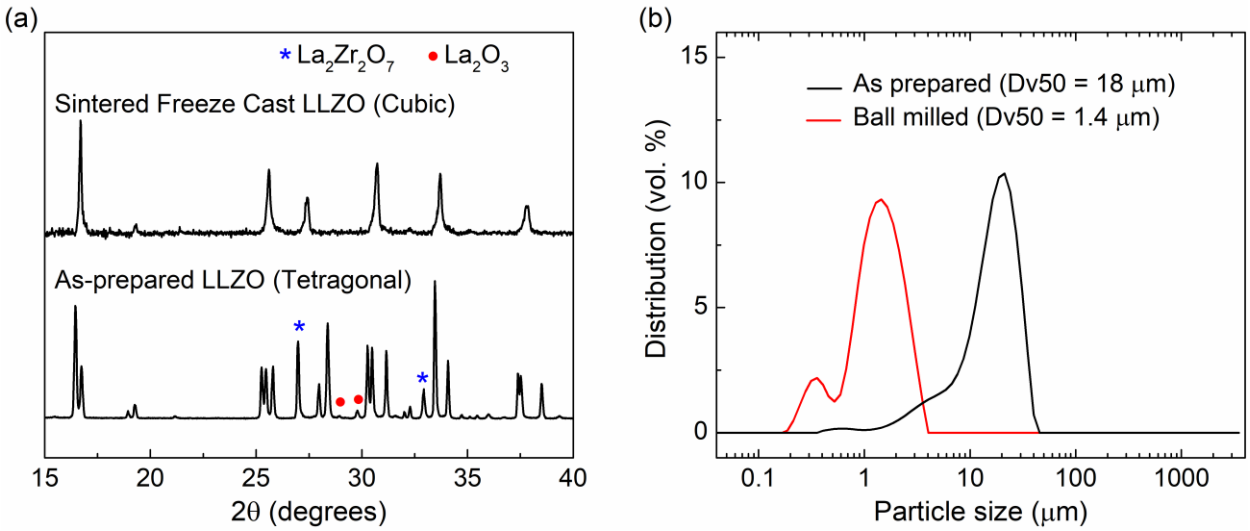

Figure 2. Characterization of the $Li_7La_3Zr_2O_{12}$ powder: (a) XRD pattern before ball-milling showing the tetragonal LLZO main phase and secondary phases and the cubic LLZO after sintering, (b) Particle size distribution of the as-prepared powder and after ball-milling.

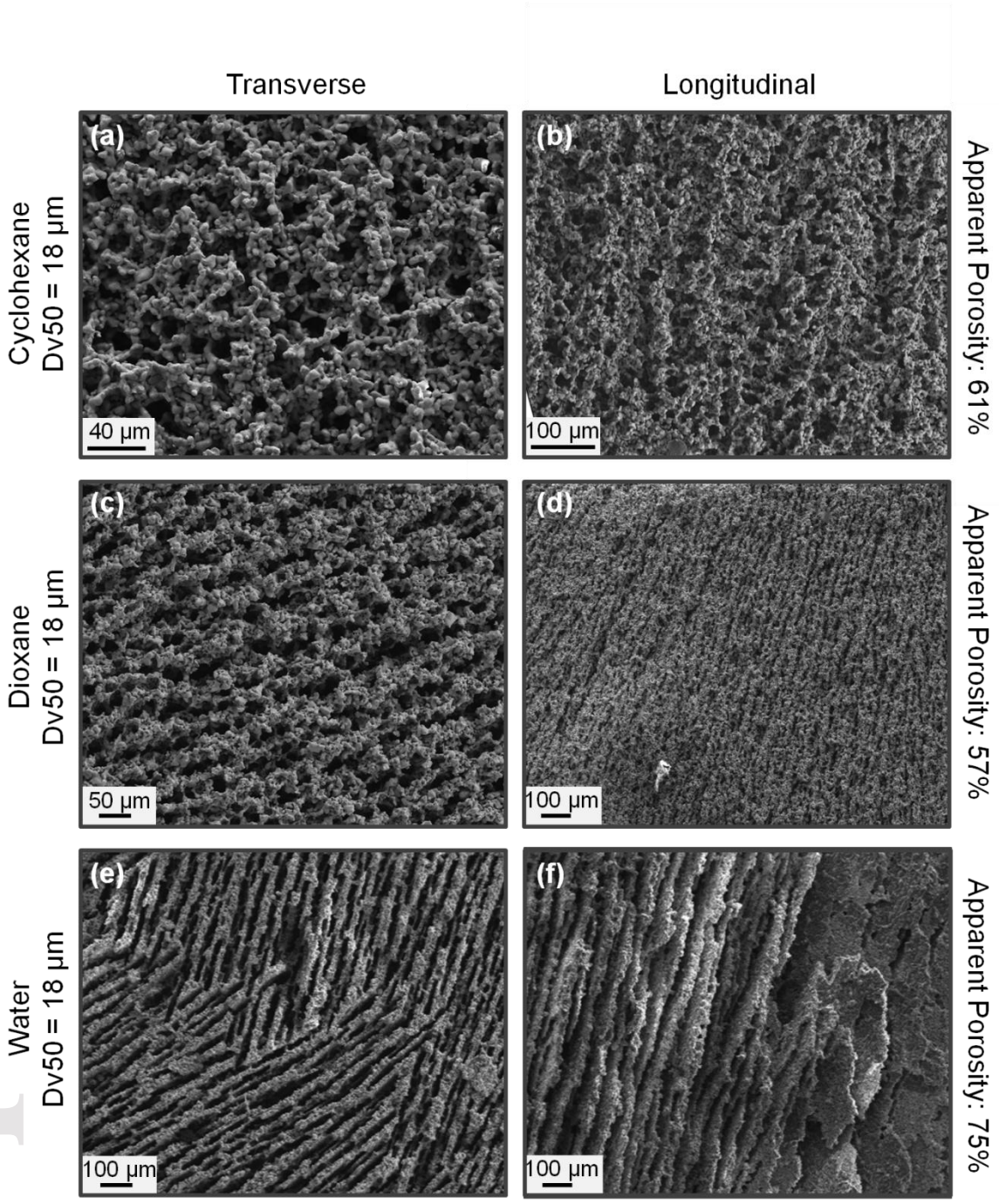

Figure 3. Effect of the solvent on the porous network of the freeze-cast $Li_7La_3Zr_2O_{12}$ solid prepared using a powder with a Dv50 of 18 µm. Transverse (a, c, e) and longitudinal (b, d, f) cross sectional SEM views of cyclohexane- (a, b), dioxane- (c, d), and water- (e, f) based slurries (20 vol.% LLZO) cooled at a rate of 3°C·min^{-1}.

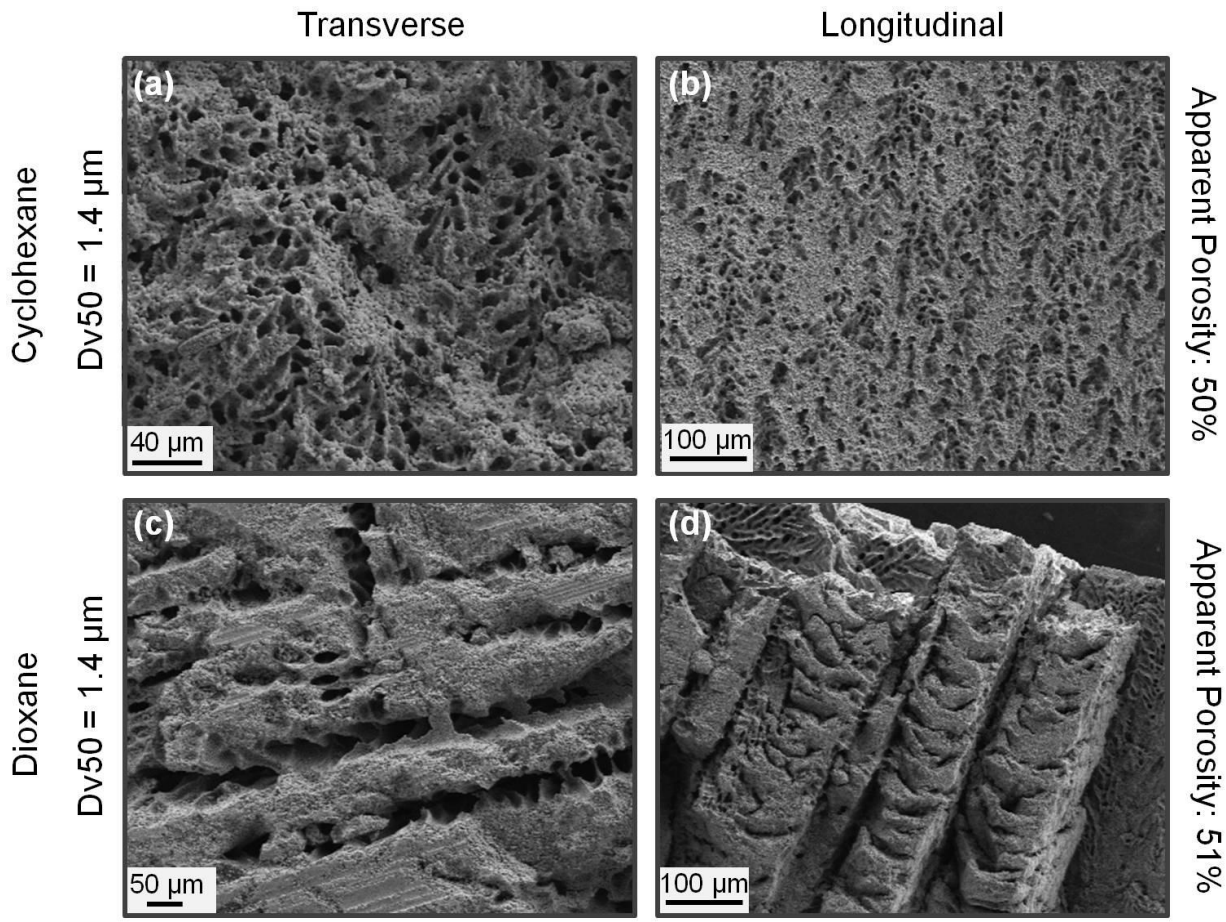

Figure 4. Effect of the particle size on the porous network of the freeze-cast $Li_7La_3Zr_2O_{12}$ solid prepared using a powder with a Dv50 of 1.4 µm. Transverse (a, c) and longitudinal (b, d) cross sectional SEM views of cyclohexane- (a, b) and dioxane- (c, d) based slurries (20 vol.% LLZO) cooled at a rate of 3°C·min^{-1}.

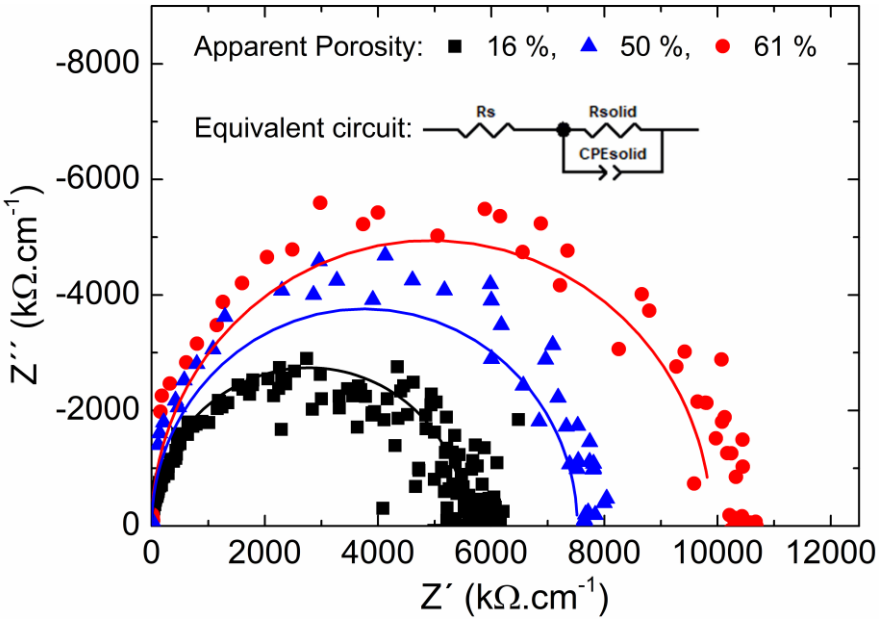

Figure 5. Electrochemical characterization of the freeze-cast LLZO solids: Nyquist plots of freeze-cast $Li_7La_3Zr_2O_{12}$ solids (red dots/line and blue triangles/line) compared to a conventional pellet (black squares/line). The symbols represent the experimental data and the solid lines correspond to the fitting using the represented model.

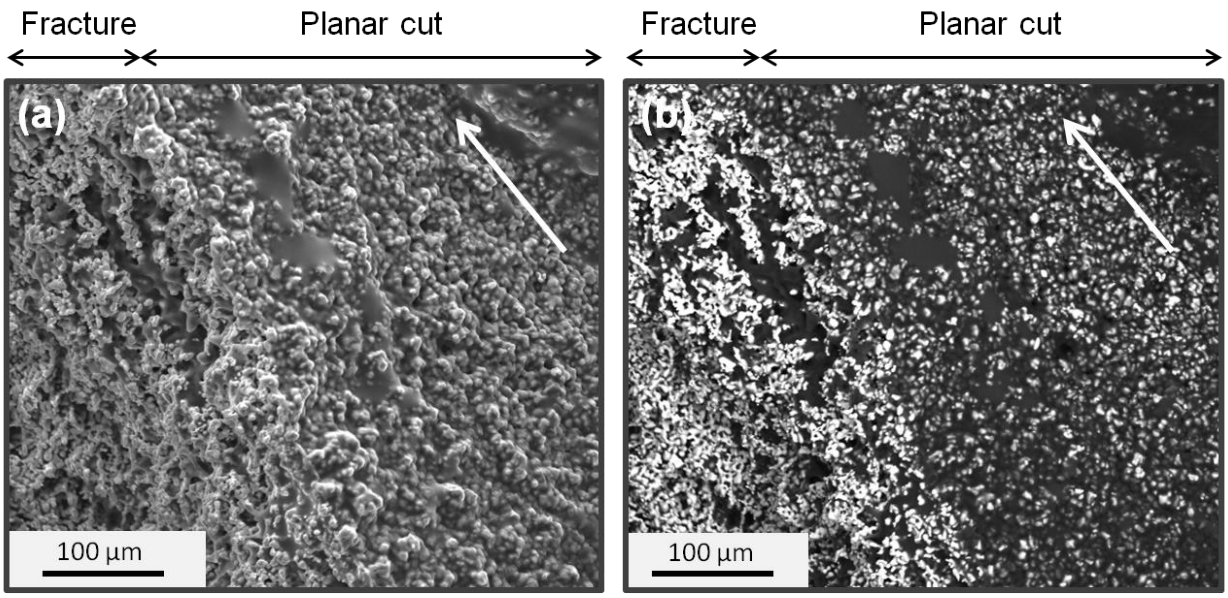

Figure 6. Longitudinal cross sectional view along a fracture surface of the polymer-infiltrated $Li_7La_3Zr_2O_{12}$ freeze-cast solid, showing the ceramic scaffold and the polymer network. Scanning electron microscopy images acquired with (a) secondary electrons and (b) backscattered electrons. The white arrow on the images indicates the freezing direction. The solid was prepared with a cyclohexane-based slurry (20 vol. % LLZ) cooled at a rate of 3°C·min^{-1}.